

ALMA sub-mm maser and dust distribution of VY Canis Majoris

A. M. S. Richards^{1,*}, C. M. V. Impellizzeri^{2,4}, E. M. Humphreys³, C. Vlahakis⁴, W. Vlemmings⁵, A. Baudry^{6,7}, E. De Beck⁵, L. Decin⁸, S. Etoka⁹, M. D. Gray¹, G. M. Harper¹⁰, T. R. Hunter², P. Kervella^{11,12,13}, F. Kerschbaum¹⁴, I. McDonald¹, G. Melnick¹⁵, S. Muller⁵, D. Neufeld¹⁶, E. O’Gorman⁵, S. Yu. Parfenov¹⁷, A. B. Peck², H. Shinnaga¹⁸, A. M. Sobolev¹⁷, L. Testi³, L. Uscanga¹⁹, A. Wootten², J. A. Yates²⁰, and A. Zijlstra¹

(Affiliations can be found after the references)

Received September 17, 2014; accepted October 16, 2014

ABSTRACT

Aims. Cool, evolved stars have copious, enriched winds. Observations have so far not fully constrained models for the shaping and acceleration of these winds. We need to understand the dynamics better, from the pulsating stellar surface to ~ 10 stellar radii, where radiation pressure on dust is fully effective. Asymmetric nebulae around some red supergiants imply the action of additional forces.

Methods. We retrieved ALMA Science Verification data providing images of sub-mm line and continuum emission from VY CMA. This enables us to locate water masers with milli-arcsec accuracy and to resolve the dusty continuum.

Results. The 658, 321, and 325 GHz masers lie in irregular, thick shells at increasing distances from the centre of expansion. For the first time this is confirmed as the stellar position, coinciding with a compact peak offset to the NW of the brightest continuum emission. The maser shells overlap but avoid each other on scales of up to 10 au. Their distribution is broadly consistent with excitation models but the conditions and kinematics are complicated by wind collisions, clumping, and asymmetries.

Key words. Stars: supergiants – Stars: individual: VY CMA – Stars: mass-loss – Masers: stars

arXiv:1409.5497v2 [astro-ph.SR] 5 Nov 2014

1. Introduction

Massive stars have a profound impact on their surroundings via their material and energy output. Observations support the importance of radiation pressure on dust in driving the stellar wind, as reviewed by Habing (1996) and confirmed for red supergiants (RSG) by Mauron & Josselin (2011). There are a variety of models for mass transport from the stellar surface to the dust formation zone at 5–10 stellar radii (R_*), based on combinations of convection (Chiavassa et al. 2011), wind levitation by pulsation and dust formation (Bowen 1988; Ireland & Scholz 2006), for example, including scattering as well as absorption (Bladh et al. 2013). Acoustic and magnetic forces were analysed by Hartmann & MacGregor (1980). However, observations do not yet confirm any of these as the dominant force. Oxygen-rich grain formation models have difficulty in explaining dust-driven winds (Woitke 2006), which can possibly be solved by the detection of large dust grains at a few R_* (Norris et al. 2012) and the complexity of the gas and dust distribution close to the photosphere (Wittkowski et al. 2007). Moreover, most investigations have focused on low-mass stars, which have a different internal structure, and despite their high mass-loss rates, RSG have irregular, often shallow periods (<http://cdsarc.u-strasbg.fr/cgi-bin/afievList?cma/vy>).

We investigated mass loss from VY CMA, one of the largest RSG, progenitor mass $\sim 25 M_\odot$, (R_*) 5.7 mas at $2 \mu\text{m}$ (Wittkowski et al. 2012), at 1.2 ± 0.1 kpc, Choi et al. 2008; Zhang et al. 2012). It has had a high and variable mass-loss rate, $0.5\text{--}1 \times 10^{-4} M_\odot \text{yr}^{-1}$ in its recent past (Decin et al. 2006), up to $3 \times 10^{-3} M_\odot \text{yr}^{-1}$ (Humphreys et al. 2007). This provides the richest-known O-rich circumstellar envelope (CSE) chemistry, as seen at sub-mm

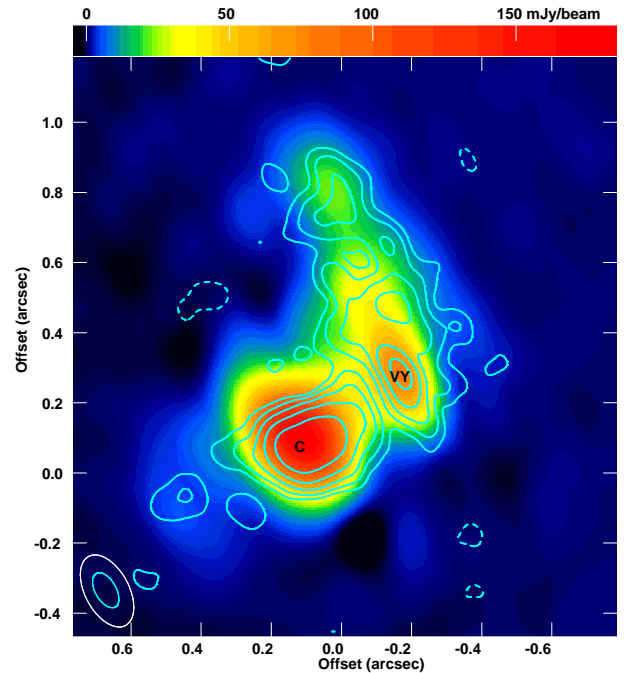


Fig. 1. Continuum emission: 321 GHz colour scale, 658 GHz contours at $(-1, 1, 2, 4, 8, 16) \times 10$ mJy beam⁻¹. Synthesized beams shown at lower left for 321 GHz (white), 658 GHz (blue). (0, 0) at R.A. 07 22 58.33454 Dec. -25 46 03.3275 (J2000). C marks the continuum peak. VY is identified as the star, at the centre of the water maser expansion.

wavelengths by *Herschel* (Alcolea et al. 2013), for instance, and imaged at $\sim 1''$ resolution using the SMA (Kamiński et al. 2013).

VY CMA has a highly asymmetric nebula that extends over a few arcsec and is shaped like a lopsided heart, irregular and

* e-mail: amsr@jb.man.ac.uk

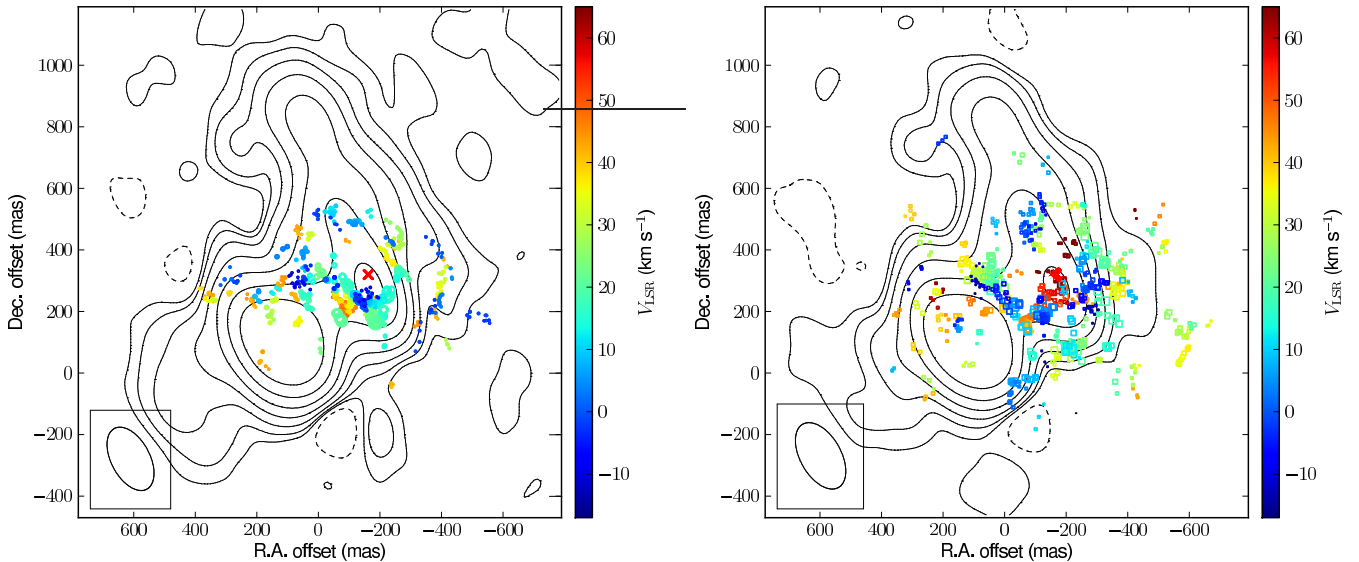


Fig. 3. 321 GHz (left) and 325 GHz (right) maser positions over continuum contours, lowest levels at $(-1, 1)$ and (-2) mJy beam $^{-1}$ at 321 and 325 GHz, respectively, and at $(2, 4, 8, 16, 32)$ mJy beam $^{-1}$ thereafter. Maser symbol size proportional to $\sqrt{\text{flux/density}}$. The red cross marks **VY**.

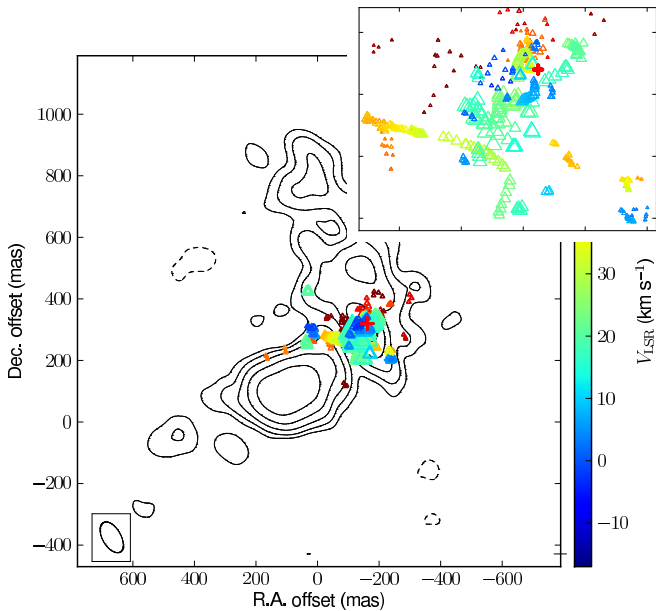


Fig. 4. 658 GHz H₂O maser positions overlying continuum contours as in Fig. 1. Maser symbols and velocity scale as in Fig. 3. The inset shows the region with bottom left and top right at $(-20, 190)$ and $(-255, 370)$ mas.

clumpy on all scales (Humphreys et al. 2007). VLA and SMA observations at 8.4–355 GHz show an unresolved central ellipse, dominated by emission from dust, (e.g. Lipsky et al. 2005; Kamiński et al. 2013). Strong OH, SiO, and 22-GHz H₂O masers have been imaged by many authors but, hitherto, there has been no astrometric confirmation that the star lies at the centre of expansion. The 22-GHz H₂O masers are located in a thick shell of radii 75–440 mas, with Doppler and proper motions dominated by accelerating outflow (Richards et al. 1998). Their maximum expansion velocity is 35.5 km s $^{-1}$ relative to the stellar velocity V_{\star} of 22 km s $^{-1}$ (all velocities are with respect to the local standard of rest, LSR).

Models (Gray 2012 and references therein; Daniel & Cernicharo 2013) predict that the 321.22564 GHz $J_{Ka,Kc} 10_{2,9}-9_{3,6}$, and possibly the 325.15292 GHz $5_{1,5}-4_{2,2}$ H₂O maser lines can emanate from conditions found at both sides of the dust formation zone. Maser emission at 321 GHz needs hotter gas than at 22 GHz, whilst lower temperatures and number densities favour 325 GHz. This has been confirmed by imaging in Cepheus A (Patel et al. 2007), but only the 22 GHz transition has ever been resolved in a CSE. The 658.00655 GHz $v_2 = 1, 1_{1,0}-1_{0,1}$ GHz maser is expected to occur very close to the star under conditions similar to SiO masers (Hunter et al. 2007). More details of these transitions are given in Table A.1. We present ALMA observations that test these predictions and, for the first time, resolve sub-mm masers, thermal lines, and continuum.

2. Data acquisition and reduction

We obtained public ALMA Science Verification data for VY CMA observed on 2013 16–19 August using 16–20 12 m antennas on baselines from 0.014–2.7 km. Three scheduling blocks (SB), covering each of the maser lines, are referred to as the 321-GHz, 325-GHz and 658-GHz SBs. The velocity resolution after Hanning smoothing is 0.45 km s $^{-1}$ at 321 and 658 GHz, and 0.9 km s $^{-1}$ at 325 GHz. More details of observations and data reduction are given in Appendix B. The fully calibrated line-free channels were imaged using a synthesized beam of $(0''.22 \times 0''.13)$ at 321 and 325 GHz, and $(0''.11 \times 0''.06)$ at 658 GHz. After subtracting the continuum, the masers were imaged using beam sizes of $(0''.18 \times 0''.09)$ and $(0''.088 \times 0''.044)$ at 321/325 and 658 GHz. We measured the positions of the masers and continuum peaks by fitting Gaussian components using the AIPS task SAD, see Appendix B.

3. VY CMA continuum and maser morphology

Before self-calibration, the positions measured by Gaussian fits to the 321 and 325 GHz peaks wandered by up to 35 mas, but at 658 GHz there were offsets of up to 100 mas, mainly due to differences between atmospheric conditions towards VY CMA and the phase reference source (see Appendix B). The 321 GHz data,

with the best atmospheric transmission and sensitivity, were used for astrometry and for continuum analysis around this frequency. The continuum at all frequencies has a similar J shape, with a bright extended peak **C**, a secondary, compact peak **VY**, and several other peaks. Shifts of $(-2, 0)$ and $(-87, 27)$ mas were applied at 325 and 658 GHz, respectively, to align **VY** with its 321 GHz position, which brought the other bright features into good positional agreement (Fig. 1). The maximum detectable angular extent in R.A. and Dec. is $1''.2 \times 1''.6$ above the $3\sigma_{\text{rms}}$ contour at 321 GHz. The 321 GHz position of **VY** is R.A. 07 22 58.3226 Dec. $-25\ 46\ 03.043$ (J2000), with 35 mas uncertainty dominated by errors in transferring phase corrections from the reference source. **VY** is 328 ± 1 mas from **C** at PA -33° . Using a matching beam size $160 \times 64 \text{ mas}^2$, **C** and **VY** had peak flux densities of 133.9 and 71.7 ($\sigma_{\text{rms}} 0.9$) mJy beam $^{-1}$ at 321 GHz and of 474 and 296 ($\sigma_{\text{rms}} 4$) mJy beam $^{-1}$ at 658 GHz. The continuum emission is analysed further by O’Gorman et al. (2014).

The total velocity extents of the H₂O lines are $(-11.9$ to $49.2)$, $(-16.8$ to $75.1)$ and $(-3.0$ to $67.7)$ km s $^{-1}$ at 321, 325, and 658 GHz. Figure 2 shows that the 325 GHz maser spectrum has the largest velocity extent and shows multiple strong peaks (similar to 22 GHz), whilst the 321 and 658 GHz spectra are dominated by single peaks, close to V_\star at 321 GHz, but 2 km s $^{-1}$ more blue-shifted at 658 GHz. Both these lines have a blue shoulder. The 325 and 658 GHz masers have a long red tail.

We estimated the brightness temperature T_b of each spatial component from its measured flux density S (Appendix B) and the beam size, that is, $T_b \geq 756S$ at 321 and 325 GHz, and $T_b \geq 3162S$ at 658 GHz. These give ranges of $(11\text{--}3.2 \times 10^5)$ K, $(46\text{--}2.0 \times 10^5)$ K, and $(444\text{--}28 \times 10^5)$ K at 321, 325, and 658 GHz. These values are lower limits since maser component sizes are probably smaller than the beam; ≤ 5 mas components would increase $T_b \gg 1000$ K in all cases, for instance. However, some of the faintest emission, especially at extreme velocities, may be genuinely extended, thermal emission from H₂O or other species.

Figures 3 and 4 show that the masers are clumped into spatially close groups at similar velocities. Much of the 321 and 658 GHz emission is concentrated in bright streamers with clear velocity gradients, for example in Fig. 4 (insert), where the long arc traces a continuum ‘valley’ between **C** and **VY**. The 325 GHz masers are more evenly distributed. There is more extended emission to the east of **VY** in all lines and brighter sub-mm masers to the south. The 321 GHz masers form a ring around **VY**; the other lines have more blue- or red-shifted emission along the line of sight to **VY** (Figs. 3–5). We estimated the centre of expansion of each line as in Richards et al. (2012), by maximising the separation between masers at close to V_\star , giving positions very close to **VY**. Figure 6 shows the angular separation of each component from **VY**, which appears to be located in a maser-free sphere. Figures 6 and 5 show that the 658, 321, and 325 GHz maser inner rims are at successively larger distances from the star, whilst the outer rims are at ~ 200 , 500, and 600 mas.

4. Discussion

VY coincides with the maser centre of expansion and is almost certainly the location of the star. This was suspected (Muller et al. 2007; Kamiński et al. 2013), but never before resolved as a distinct continuum peak. Our position (Sect. 3) agrees within the uncertainties with the centre of expansion of SiO and 22 GHz H₂O masers (Zhang et al. 2012; Choi et al. 2008).

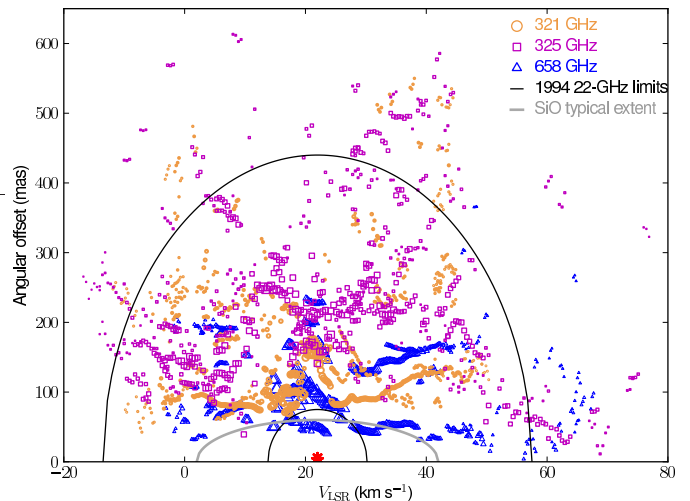


Fig. 6. Symbols mark sub-mm H₂O maser component angular separations from **VY** as a function of V_{LSR} . The black and grey lines mark the inner and outer limits of 22 GHz H₂O masers and the outer rim of J=1–0 and J=2–1 SiO masers.

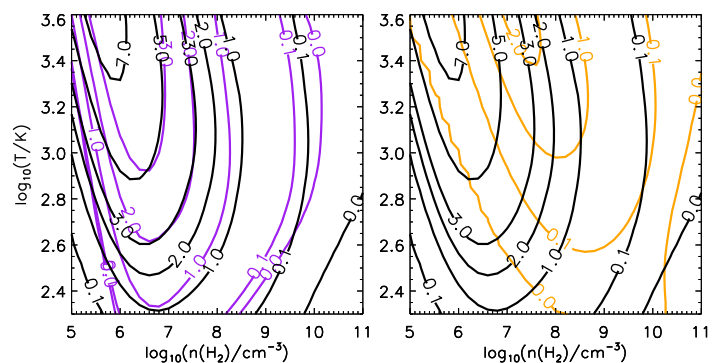


Fig. 8. Maser (negative) optical depths for 22 GHz (black, both panels), 325 GHz masers (magenta, left panel) and 321 GHz (orange, right panel). Amplification occurs if this exceeds zero.

Exponential maser amplification exaggerates small differences in conditions, so single-epoch data are interpreted with caution. The 658 GHz masers have a complex distribution close to the star, but mostly outside the typical SiO outer rim, taken from Richter et al. (2013), as shown in Fig. 6 (although Shinaga et al. (2004) found a more extended bipolar outflow). The asymmetric emission at large angular separations and expansion velocities (Fig. 6) is inconsistent with a simple velocity-radius relationship. The inner 658 GHz masers arise in the pulsation-dominated region, but straddle the dust formation zone identified by Decin et al. (2006) and indicated by the 22 GHz inner radius.

The patchy ring of bright 321 and 325 GHz masers within ~ 10 km s $^{-1}$ of V_\star (Fig. 3) is typical of tangential beaming from a radially accelerating shell. The 321 GHz masers are undetectable towards the star, suggesting that they trace particularly strongly accelerated gas. The red- and blue-shifted emission at large angular separations suggests additional, complex motions. The brightest 325 GHz masers occur at velocities close to V_\star , seen in Fig. 7, but asymmetries are seen in the south and east offsets of the moderately blue- and red-shifted peaks. Figures 3 and 4 suggest that the masers, especially at 658 GHz, trace shocks where the stellar wind encounters continuum peak **C**. Elongated, bright maser features characteristic of shocks, seen at up to ~ 150 mas from the star, could be associated with dust

formation (Bladh et al. 2013) or wind collisions arising from inhomogeneous mass loss/speeds (Zijlstra et al. 2001).

We grouped the maser components into features and attempted to cross-match the clumps of different transitions, but found no significant associations, so co-propagation of these sub-mm masers seems unlikely. A comparison with 22 GHz was not made because of the difference in epochs; around similar evolved stars these are concentrated in clumps with a filling factor $\lesssim 1\%$, containing 30–90% of the total mass loss in this region (Richards et al. 2012), embedded in less dense gas.

The lines studied arise from distinct, although overlapping zones, and are segregated on scales of a few tens of au. All are thought to be collisionally pumped (Yates et al. 1997). Figure 8 compares the physical conditions required for masing of the three vibrational ground-state lines using an excitation model similar to that described by Neufeld & Melnick (1991) updated as detailed in Appendix C. The conditions in the VY CMA CSE lie around the locus from top right (near the star) to bottom left, but with a variation of up to $\times 70$ in number density and $\times 0.7$ in temperature in denser clumps or compressed material. The contours mark the negative optical depths in the direction of the velocity gradient for unsaturated masers; the optical depths in other directions may greatly exceed the values shown here (optical depths of 22 GHz masers have been estimated at up to ~ 13 in RSG S Per, Richards et al. 2011). The 321 GHz gain drops rapidly below 1000 K, whilst the 22 and 325 GHz masers extend to cooler temperatures. The 325 GHz maser is collisionally quenched at lower densities than the 22 GHz and 321 GHz transitions.

The models of Humphreys et al. (2001) predicted a comparable radial range for 22 and 325 GHz masers around low-mass stars, the latter being favoured in cooler, more rarefied conditions, possibly in a two-phase medium. These predictions agree well with the observed inner radii at successively higher distances from the star at 321, 22, and 325 GHz, if the inner radii of 321 and 325 GHz masers are determined by conditions in the inter-clump gas surrounding the 22 GHz clouds. Not yet published models (Gray) require temperatures > 1500 K and H_2 number densities $\sim 6 \times 10^9 \text{ cm}^{-3}$ for 658 GHz masers, likely to be found in the inner parts of its observed distribution, but the more extended emission is surprising. The excitation of 321 GHz masers at 500 mas (600 au) from the star is also puzzling since typical temperatures of 250 K (Decin et al. 2006) are too low, so local heating might be important.

5. Summary

These ALMA observations have identified the centre of expansion of high-excitation masers with a distinct continuum peak, VY CMA itself, 360 au NW of the brightest sub-mm dust emission. The 658, 321, and 325 GHz masers are found at increasing distances from the star as predicted, but reach unexpectedly large separations. The high-excitation 658 and possibly 321 GHz masers cross the dust formation zone and some emission appears to emanate from shocked regions surrounding the star and tracing the limbs of C; interaction with the uniquely complex dust distribution is undoubtedly significant. The different transitions form clumps that do not overlap even when found at similar separations from VY. The velocities are generally consistent with expansion but deviate drastically and irregularly from spherical symmetry. We will compare the maser kinematics with models of a flared disc plus bipolar outflow (Decin et al. 2006; Muller et al. 2007) and ejection along less symmetric arcs as described by Humphreys et al. (2007). These observations provide the first opportunity to test sub-mm maser models rigorously, to

be followed-up in future papers along with an analysis of the kinematics, thermal lines, and dust.

Acknowledgements. This paper makes use of ALMA data: ADS/JAO.ALMA #2011.0.00011.SV. ALMA is a partnership of ESO (representing its member states), NSF (USA) and NINS (Japan), together with NRC (Canada) and NSC and ASIAA (Taiwan), in cooperation with the Republic of Chile. The Joint ALMA Observatory is operated by ESO, AUI/NRAO and NAOJ. We thank the anonymous referee for thoughtful comments that have greatly improved the clarity of this paper.

References

- Alcolea, J., Bujarrabal, V., Planesas, P., et al. 2013, *A&A*, 559, A93
- Bladh, S., Höfner, S., Nowotny, W., Aringer, B., & Eriksson, K. 2013, *A&A*, 553, A20
- Bowen, G. H. 1988, *ApJ*, 329, 299
- Chiavassa, A., Freytag, B., Masseron, T., & Plez, B. 2011, *A&A*, 535, A22
- Choi, Y. K., Hirota, T., Honma, M., et al. 2008, *PASJ*, 60, 1007
- Daniel, F. & Cernicharo, J. 2013, *A&A*, 553, A70
- Decin, L., Hony, S., de Koter, A., et al. 2006, *A&A*, 456, 549
- Gray, M. 2012, *Maser Sources in Astrophysics* (Cambridge University Press)
- Habing, H. J. 1996, *A&A Rev.*, 7, 97
- Hartmann, L. & MacGregor, K. B. 1980, *ApJ*, 242, 260
- Humphreys, E. M. L., Yates, J. A., Gray, M. D., Field, D., & Bowen, G. H. 2001, *A&A*, 379, 501
- Humphreys, R. M., Helton, L. A., & Jones, T. J. 2007, *AJ*, 133, 2716
- Hunter, T. R., Young, K. H., Christensen, R. D., & Gurwell, M. A. 2007, in *IAU Symposium*, ed. J. M. Chapman & W. A. Baan, Vol. 242, 481–488
- Ireland, M. J. & Scholz, M. 2006, *MNRAS*, 367, 1585
- Kamiński, T., Gottlieb, C. A., Young, K. H., Menten, K. M., & Patel, N. A. 2013, *ApJS*, 209, 38
- Lipscy, S. J., Jura, M., & Reid, M. J. 2005, *ApJ*, 626, 439
- Mauron, N. & Josselin, E. 2011, *A&A*, 526, A156
- Muller, S., Dinh-V-Trung, Lim, J., et al. 2007, *ApJ*, 656, 1109
- Neufeld, D. A. & Melnick, G. J. 1991, *ApJ*, 368, 215
- Norris, B. R. M., Tuthill, P. G., Ireland, M. J., et al. 2012, *Nat.*, 484, 220
- O’Gorman, E., Vlemmings, W., Richards, A. M. S., et al. 2014, *ArXiv e-prints*
- Patel, N. A., Curiel, S., Zhang, Q., et al. 2007, *ApJ*, 658, L55
- Richards, A. M. S., Elitzur, M., & Yates, J. A. 2011, *A&A*, 525, A56
- Richards, A. M. S., Etoka, S., Gray, M. D., et al. 2012, *A&A*, 546, A16
- Richards, A. M. S., Yates, J. A., & Cohen, R. J. 1998, *MNRAS*, 299, 319
- Richter, L., Kemball, A., & Jonas, J. 2013, *MNRAS*, 436, 1708
- Shinnaga, H., Moran, J. M., Young, K. H., & Ho, P. T. P. 2004, *ApJ*, 616, L47
- Witkowski, M., Boboltz, D. A., Ohnaka, K., Driebe, T., & Scholz, M. 2007, *A&A*, 470, 191
- Witkowski, M., Hauschildt, P. H., Arroyo-Torres, B., & Marcaide, J. M. 2012, *A&A*, 540, L12
- Woitke, P. 2006, *A&A*, 460, L9
- Yates, J. A., Field, D., & Gray, M. D. 1997, *MNRAS*, 285, 383
- Zhang, B., Reid, M. J., Menten, K. M., & Zheng, X. W. 2012, *ApJ*, 744, 23
- Zijlstra, A. A., te Lintel Hekkert, P., Chapman, J. M., et al. 2001, *MNRAS*, 322, 280

-
- ¹ JBCA, School of Physics and Astronomy, Univ. of Manchester, UK
 - ² NRAO, 520 Edgemont Road, Charlottesville, VA22903, USA
 - ³ ESO Karl-Schwarzschild-Str. 2, 85748 Garching, Germany
 - ⁴ Joint ALMA Observatory/European Southern Observatory, Alonso de Cordova 3107, Vitacura, Santiago, Chile
 - ⁵ Department of Earth and Space Sciences, Chalmers University of Technology, Onsala Space Observatory, SE 439 92 Onsala, Sweden
 - ⁶ Univ. Bordeaux, LAB, UMR 5804, F-33270 Floirac, France
 - ⁷ CNRS, LAB, UMR 5804, F-33270 Floirac, France
 - ⁸ Instituut voor Sterrenkunde, Katholieke Universiteit Leuven, Celestijnenlaan 200D, 3001 Leuven, Belgium
 - ⁹ Hamburger Sternwarte, Univ. of Hamburg, Gojenbergsweg 112, D-21029 Hamburg, Hamburg, Germany
 - ¹⁰ School of Physics, Trinity College Dublin, Ireland
 - ¹¹ LESIA, Observatoire de Paris, CNRS, UPMC, Université Paris-Diderot, PSL, 5 place Jules Janssen, 92195 Meudon, France
 - ¹² UMI-FCA, CNRS/INSU, France (UMI 3386)
 - ¹³ Dept. de Astronomía, Universidad de Chile, Santiago, Chile
 - ¹⁴ Dept. of Astrophysics, Univ. of Vienna, Türkenschanzstraße 17, 1180, Vienna, Austria
 - ¹⁵ Harvard-Smithsonian Center for Astrophysics, 60 Garden Street, MS 66, Cambridge, MA 02138, USA
 - ¹⁶ Dept. of Physics & Astronomy, Johns Hopkins Univ. 3400 North Charles Street, Baltimore, MD 21218, USA
 - ¹⁷ Ural Federal University, Ekaterinburg, Russia
 - ¹⁸ NAOJ, 2-21-1 Osawa, Mitaka, Tokyo, Japan zip 181-8588
 - ¹⁹ IAASARS, National Observatory of Athens, 15236 Athens, Greece
 - ²⁰ Dept. of Physics and Astronomy, University College London, WC1E 6BT, UK

Table A.1. H₂O masers. ν_2 : vibrational state; spin: ortho/para isomers.

Frequency (GHz)	Transition ($J_{Ka,Kc}$)	ν_2	E_U (K)	Spin (level)	Discovery (reference)
22.23508	6 _{1,6} –5 _{2,3}	0	643	<i>o</i>	C69
321.22564	10 _{2,9} –9 _{3,6}	0	1862	<i>o</i>	M90
325.15292	5 _{1,5} –4 _{2,2}	0	470	<i>p</i>	M91
658.00655	1 _{1,0} –1 _{0,1}	1	2361	<i>o</i>	M95

References. C69 Cheung et al. (1969); M90 Menten et al. (1990); M91 Menten & Melnick (1991); M95 Menten & Young (1995).

Table B.1. Observational parameters. $\Delta_{\nu\text{cont}}$: effective continuum bandwidth for the whole SB, giving noise $\sigma_{\text{rms cont}}$. $\delta\nu$: unaveraged channel spacing; σ_{rms1} : noise in 1 km s⁻¹ channels free from bright emission.

SB (GHz)	spw centre (GHz)	spw width (GHz)	$\Delta_{\nu\text{cont}}$ (GHz)	$\sigma_{\text{rms cont}}$ (mJy)	$\delta\nu$ (kHz)	σ_{rms1} (mJy)
321	321.18305	0.9375	1.74	0.31	244.141	2.5
321	322.44385	0.9375			244.141	2.5
321	310.95845	0.9375			244.141	1.6
321	309.95865	0.9375			244.141	1.7
325	325.10740	1.873	2.25	1.1	488.281	7.5
325	321.96140	1.873			488.281	1.8
658	657.82750	1.872	0.4	2.4	488.281	20

Appendix A: Water maser lines

Table A.1 gives some properties of the sub-mm maser lines resolved by ALMA and the well-known 22 GHz maser.

Appendix B: Observations and data processing

VY CMA was observed by ALMA on 2013 16–19 August using 16–20 12 m antennas. The primary objective of these Science Verification (SV) observations was to demonstrate the ability to observe on baselines up to 2.7 km and develop calibration techniques involving strong, narrow spectral lines. Three separate configurations or scheduling blocks (SBs), covering each of the maser lines, are referred to as the 321 GHz, 325 GHz, and 658 GHz SBs; details are given in Table B.1. These were divided into one or more spectral windows (spw) covering ~850–1700 km s⁻¹ (depending on SB). Each spw was divided into 3840 channels, but as a result of Hanning smoothing in the correlator, the finest effective velocity resolution is approximately double the channel spacing, that is, 0.45 km s⁻¹ for 321 and 658 GHz, and 0.9 km s⁻¹ at 325 GHz. The data and scripts (including a description of the procedures) used for calibration and initial imaging are available from <http://almascience.eso.org/alma-data/science-verification>. As a Science Verification project, some observational methods were experimental, for example the duration of phase-referencing cycles turned out to allow a few phase ambiguities at the highest frequencies. Methods such as band-to-band phase transfer and fast switching will be available in future. These observations required very dry atmospheric conditions, so the weather determined their duration within the time available for Science Verification. Normal ALMA calibration and imaging procedures were followed, using CASA (<http://casa.nrao.edu>). Each SB was executed three times at different hour angles, giving a total time on VY CMA at each frequency of ~1.5 hr in addition to calibration observations. The phase-reference source J0648-3044 was observed in 1.5 min scans, bracketing 6.75 min on VY CMA for the 321 GHz SB and 5.25 min for the 325 and 658 GHz SBs.

Antenna positions were updated where required, and applied corrections derived from system temperature and water vapour radiometry measurements. The precipitable water vapour (PWV) was 0.3 mm except for the last of the three 658 GHz observations, when it was 0.7 mm. The water vapour radiometry corrections produced very significant improvements, especially for the 658 SB taken at 0.7 mm PWV. A small amount of bad data were excised.

The bright QSO J0522-3627 was used for bandpass calibration. This was observed for the default duration of 5.25 min in each of the three executions of the 321 GHz SB. However, it was only observed for 2.5 min in each of the 325 GHz and 658GHz SBs. After all calibration was complete, we checked the variation of the imaged continuum emission with frequency within each SB. The channel-to-channel position scatter was as expected from the signal-to-noise ratio (S/N), without any systematic position shift, and the flux density was consistent with the expected spectral index ~-2, so we are satisfied that the bandpass does not lead to misleading results. The main symptom was that the noise rms decreased more shallowly than the expected inverse square-root dependence on the number of channels averaged. The position uncertainties were also affected by dynamic range limitations in imaging and by possibly incomplete modelling of the atmosphere in the deep water-absorption lines.

Pallas was used as the primary flux scale calibrator (Butler-JPL-Horizons 2012, ALMA Memo 594), selecting baselines shorter than the first null in the visibilities. Using the 321 GHz SB, the flux density derived from Pallas for the phase-reference source, J0648-3044, was 0.433 ± 0.008 Jy at reference frequency 316.093 GHz, spectral index $\alpha -0.80 \pm 0.03$. Since the 325 GHz data covered similar frequencies but had a poorer S/N than the 321-GHz data, we extrapolated the 321 GHz values to the relevant frequencies for the 325 GHz data. At 658 GHz, the flux density of J0648-3044 derived from Pallas is 0.28 Jy, compared with 0.24 ± 0.02 Jy extrapolated from 321 GHz. This may not be a fair comparison, since there is no guarantee that the spectral index is linear from 321 to 658 GHz, but it suggests that the error could be up to 15%.

The phase-reference source, J0648-3044, 9° from VY CMA, was used to derive time-dependent phase and amplitude corrections. The phase could be connected smoothly between successive scans for most antennas and times, but in a few cases where there was an ambiguity, the target scan affected was excluded from the initial imaging.

After applying instrumental and calibration source corrections, the VY CMA data in each SB was adjusted to constant velocity with respect to the Local Standard of Rest (LSR). All velocities are given as V_{LSR} . Low-resolution cubes were made for each data set to identify line-free continuum, and we made preliminary images to check the astrometry. In each SB, the brightest maser channel was identified and imaged, providing a starting model for self-calibration. After several iterations, the solutions were applied to all channels. The solutions were applied to all channels and to the data initially excluded because of the phase-referencing ambiguities noted above.

The bandwidth corresponding to the sum of line-free channels (spread over the whole observing bandwidth) $\Delta_{\nu\text{cont}}$ and the image noise rms $\sigma_{\text{rms cont}}$ are given in Table B.1. The mean frequencies were 316 and 319 GHz for the data sets referred to as 321 and 325 GHz. The continuum channels were imaged using natural weighting, which gave a synthesised beam of (0′22×0′13) at 321 and 325 GHz, and (0′11×0′06) at 658 GHz. In all cases the beam position angle (PA) was ~28°.

The shortest baseline was 14 m, and inspection of the visibility amplitudes against baseline length shows that the flux density remains quite steady out to 70 m at 658 GHz and 170 m at 321–325 GHz, suggesting that we recover all the flux on scales $< 6''$ or $< 13''$ at the higher or lower frequencies. We compared the total continuum flux densities with literature values (Fu et al 2012; Kamiński et al. 2013; Muller et al. 2007; Shinnaga et al. 2004). All the measurements using $\sim 1''$ aperture lie close to a spectral index of 2.2 ± 0.2 . Those taken using a larger aperture, such as at 658-GHz from Shinnaga et al. (2004) and by Knapp & Woodhams (1993) using the JCMT (effective aperture $\sim 18''$), are higher, for instance 0.62 ± 0.04 Jy at 240 GHz, 2.18 ± 0.24 Jy at 353 GHz and 9.7 ± 1.5 Jy at 677 GHz. This suggests that there is an extended component of dust on scales larger than we sampled.

The continuum was subtracted from each data set and partial uniform weighting (Briggs weighting with $\text{robust}=0.5$ as defined by CASA) was used to image the masers, giving beam sizes of $(0''.18 \times 0''.09)$ and $(0''.088 \times 0''.044)$ at 321/325 and 658 GHz, respectively. No spectral averaging was applied, so the measurements for each maser channel are not completely independent as a result of the Hanning smoothing in the correlator. All image extents were $\leq 80\%$ of the primary beam, so no primary beam correction was applied.

The maser peak brightnesses and S/N in each of the cubes were 321 GHz: 426.6 Jy beam $^{-1}$, S/N 2010; 325 GHz: 271 Jy beam $^{-1}$, S/N 1330; 658 GHz: 361 Jy beam $^{-1}$, and S/N 764. In the maser line wings (not dynamic-range limited but affected by the atmosphere) the σ_{rms} noise values were 4, 15, and 40 mJy for 321, 325, and 658 GHz, respectively. The values for all spw at lower resolution are given in Table B.1.

We measured the positions of the masers and continuum peaks by fitting two-dimensional Gaussian components using the AIPS task SAD. We did not attempt to resolve the individual components since the smallest beam size ~ 50 mas is much larger than the probable maser beamed size, although this might be possible for the brightest masers. Thus all flux densities are measured over the restoring beam. The relative position uncertainties are given by (beam size)/S/N (for fairly sparse uv coverage in narrow channels (Condon et al. 1998; Richards 1997). We selected components $> 3\sigma_{\text{rms}}$ at 321 and 325 GHz or $> 4\sigma_{\text{rms}}$ at 658 GHz (where σ_{rms} was measured separately off-source for each channel) and rejected those that obviously coincided with sidelobes. We rejected components that did not form series of at least three in successive channels, within the maximum position uncertainty.

The total flux in fitted maser components at 321, 325, and 658 GHz is 95%, 65%, and 76% of the integrated map flux density for each SB. However, the fraction of flux recovered in components is no higher for channels containing peaks > 100 Jy, implying that the main loss is due to deconvolution errors putting power into sidelobes, since the 325 and 658 GHz masers are more affected by atmospheric conditions. The component selection method avoids locating spurious positions, at the expense of loss of peak flux. We grouped the maser components into features comprising series of components in successive channels within the position errors, as in Richards et al. (2012), and attempted to cross-match the clumps of different transitions but found no significant associations. In each case, 5–10% of features have pairs within 50 mas, 2 km s^{-1} , but applying a 50 mas shift to one data set produces a similar number of pairs, so this seems like random coincidence.

Appendix C: Maser modelling

Figure 8 compares the physical conditions needed to excite the observed maser transitions (at 22 GHz and 321 and 325 GHz) within the ground-vibrational state. Here, we present results obtained with an excitation model that included the combined effects of collisional excitation by H_2 , spontaneous radiative decay, and radiative trapping of infrared transitions. We adopted the latest quantal rate coefficients (Daniel et al. 2011) for collisionally induced transitions amongst the lowest 45 rotational states of ortho- and para- H_2O , together with an extrapolation (Neufeld 2010) to the next 75 rotational states. We treated the effects of radiative trapping with the use of an escape probability method and the assumption of a steep velocity gradient in a single direction (e.g. Neufeld & Melnick 1991). The results plotted here are for an effective water column density, $N(\text{H}_2\text{O}) = n(\text{H}_2\text{O})/(dv/dz)$ of $10^{17} \text{ cm}^{-2} \text{ per km s}^{-1}$; based upon the density and velocity profiles obtained for VY CMa by Decin et al. (2006), this value is appropriate for the general outflow at distances in the range 150 to 750 au, corresponding to angular offsets of 125 to 625 mas (the region within which most of the maser spots are located). The plotted contours show, as a function of temperature and H_2 density, the negative optical depths predicted in the direction of the velocity gradient. These optical depths were computed in the unsaturated limit, where the population inversion is assumed to be undiminished by the effects of stimulated emission.

The contours labelled zero mark the boundary of the region within which the level populations are inverted. That region covers a broad range of densities and temperatures for all three transitions considered, although the 321 GHz maser gain drops rapidly below ~ 1000 K, as expected given its relatively high upper state energy. Similar calculations, not presented here, for the 658 GHz transition show a similar behaviour; this transition, too, shows a significant maser gain only at high temperature. Clearly, in the limit of high density, the population inversion for any transition inevitably disappears as the level populations approach LTE. However, the quenching density above which the population inversion vanishes varies from transition to transition and is clearly lowest for the 325 GHz transition. This behaviour may explain why the 325 GHz spots, as plotted in Figure 5 (purple squares), have a larger inner boundary than the other masing transitions.

Despite the large overlap of the regions in parameter space within which strong maser amplification can occur (Fig. 8), there are few or no exact coincidences between the 321 and 325 GHz maser spots observed simultaneously. As noted previously, this may simply reflect the tendency of the exponential amplification process to accentuate small differences in opacity.

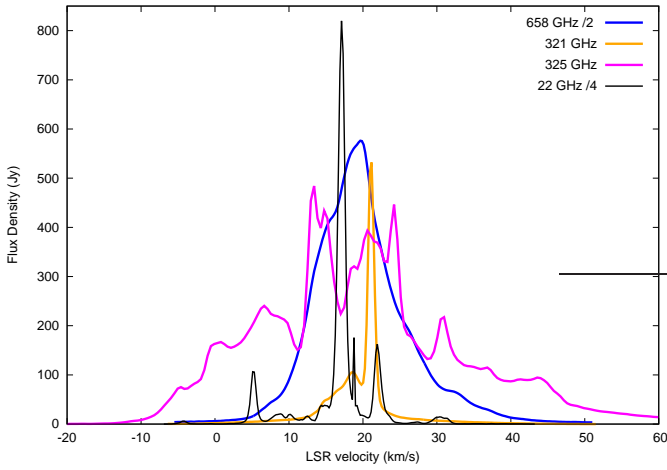


Fig. 2. Integrated water maser spectra, derived from the interferometric image cubes, measured in square boxes of width $0''.75$, $1''.0$ and $0''.4$ at 321, 325, and 658 GHz, centred on **VY**. The 658 GHz spectrum is scaled by 0.5 and the 22 GHz spectrum by 0.25.

References (Appendix)

- Cheung, A. C., Rank, D. M., Townes, C. H., Thornton, D. D., & Welch, W. J. 1969, *Nat*, 221, 626
- Condon, J. J., Cotton, W. D., Greisen, E. W., et al. 1998, *AJ*, 115, 1693
- Daniel, F., Dubernet, M.-L., & Grosjean, A. 2011, *A&A*, 536, A76
- Decin, L., Hony, S., de Koter, A., et al. 2006, *A&A*, 456, 549
- Fu, R. R., Moullet, A., Patel, N. A., et al. 2012, *ApJ*, 746, 42
- Kamiński, T., Gottlieb, C. A., Young, K. H., Menten, K. M., & Patel, N. A. 2013, *ApJS*, 209, 38
- Knapp, G. R. & Woodhams, M. 1993, in *Massive Stars: Their Lives in the Interstellar Medium*, ed. J. P. Cassinelli & E. B. Churchwell, Vol. 35 (ASP conference series, San Francisco), 199
- Menten, K. M. & Melnick, G. J. 1991, *ApJ*, 377, 647
- Menten, K. M., Melnick, G. J., & Phillips, T. G. 1991, *ApJ*, 350, L41
- Menten, K. M. & Young, K. 1995, *ApJ*, 450, L67
- Muller, S., Dinh-V-Trung, Lim, J., et al. 2007, *ApJ*, 656, 1109
- Neufeld, D. A. 2010, *ApJ*, 708, 635
- Neufeld, D. A. & Melnick, G. J. 1991, *ApJ*, 368, 215
- Richards, A. M. S. 1997, PhD thesis, University of Manchester
- Richards, A. M. S., Etoke, S., Gray, M. D., et al. 2012, *A&A*, 546, A16
- Shinnaga, H., Moran, J. M., Young, K. H., & Ho, P. T. P. 2004, *ApJ*, 616, L47

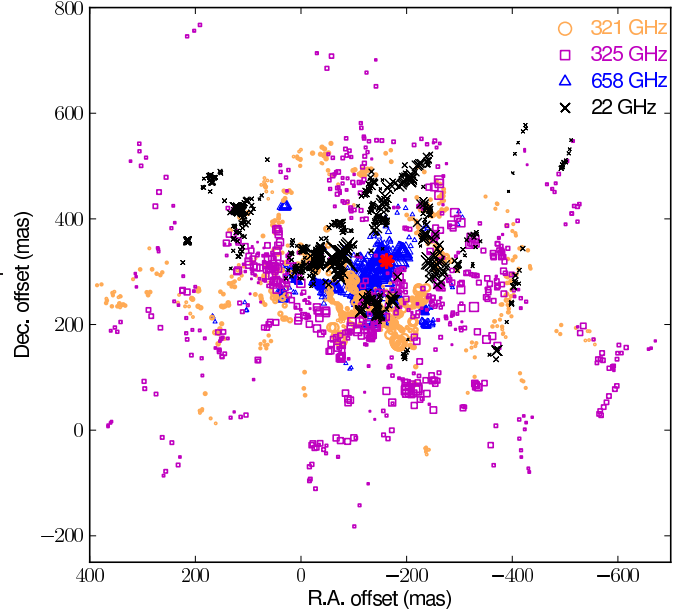


Fig. 5. Relative positions of all imaged maser components.

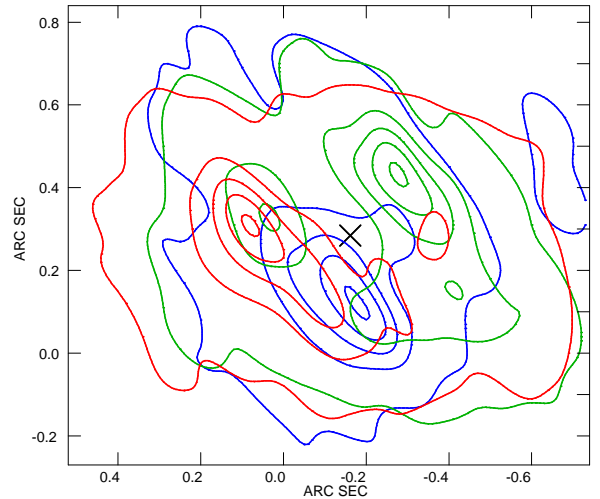


Fig. 7. 325 GHz masers, summed over <17 , $17\text{--}27$, and >27 km s^{-1} , shown in blue, green, and red. Contour levels start at 30 Jy; higher levels are at 24%, 48%, 72%, and 96% of the peak, where the peak is 2184, 1018, and 903 Jy for the red, green, and blue ranges. These levels have been chosen to emphasise the brighter emission and indicate the total extent at a uniform sensitivity limit (to 1–3% peak), omitting fine details. The cross marks **VY**.